Energy Storage Materials 72 (2024) 103735

Contents lists available at ScienceDirect

Energy Storage Materials

journal homepage: www.elsevier.com/locate/ensm

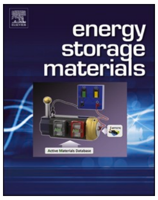

Sulfonyl diimidazole to stabilize fluoroethylene carbonate-based SEI in high-voltage Li ion cells with a SiO_x containing negative electrode

Feleke Demelash [a], Anindityo Arifiadi [a,b], Bastian Heidrich [a], Egy Adhitama [a], Christian-Timo Lechtenfeld [a], Niklas M. Abke [a], Matthias Weiling [c], Jian Fen Wang [c], Diddo Diddens [c], Simon Wiemers-Meyer [a], Martin Winter [a,c], Masoud Baghernejad [c], Philip Niehoff [a,*]

[a] University of Münster, MEET Battery Research Center, Institute of Physical Chemistry, Corrensstr. 46, Münster 48149, Germany
[b] University of Münster, International Graduate School for Battery Chemistry, Characterization, Analysis, Recycling and Application (BACCARA), Corrensstr. 40, Münster 48149, Germany
[c] Helmholtz Institute Münster, IEK-12, Forschungszentrum Jülich GmbH, Corrensstr. 46, Münster 48149, Germany

ARTICLE INFO

Keywords:
LIB
Roll over
SEI
TMD
Additive

ABSTRACT

Pairing nickel-rich layered oxide cathodes (*e.g.*, $LiNi_{0.8}Mn_{0.1}Co_{0.1}O_2$ (NMC811)) with silicon-based anodes (*e.g.*, SiO_x-graphite) and simultaneously increasing the upper cut-off voltage ($>$ 4.3 V vs. $Li|Li^+$) offers a promising pathway to increase the energy density of LIBs. However, the instability of state-of-the-art electrolytes poses a notable challenge for high-voltage Li ion cells with SiO_x-based anodes due to abrupt cell failure. This challenge originates mainly from the restricted lithium transport due to a thick solid electrolyte interphase (SEI), followed by lithium metal plating on the SiO_x-Gr anode, which leads to a roll-over failure. In this study, we introduce an additive-based electrolyte designed to facilitate the formation of a stable SEI on SiO_x-Gr while protecting the SEI from attack by hydrofluoric acid and PF_6^-. The electrolyte formulation comprises 1 M lithium hexafluorophosphate ($LiPF_6$) dissolved in ethyl carbonate (EC) and ethyl methyl carbonate (EMC) mixture (3:7 by wt.) with 5 wt.% fluoroethylene carbonate (FEC) and 1.5 wt.% sulfonyl diimidazole show the ability to suppress roll-over behavior and retain a capacity of 92 % at 1C and 20 °C.

1. Introduction

Considerable efforts have been put into increasing the energy density of Li ion batteries (LIBs), to enable long-range and affordable electric vehicles [1–4]. Achieving high energy density is possible by employing nickel-rich layered oxide cathodes such as $LiNi_{0.8}Mn_{0.1}Co_{0.1}O_2$ (NMC811). Further enhancement of energy density is attainable by elevating the upper cut-off voltage (UCV) due to the higher degree of lithium extraction from the cathode associated with a higher cell voltage [5–7]. Nevertheless, raising the UCV is followed by structural degradation, electrolyte oxidation, and subsequent formation of a resistive cathode-electrolyte interphase (CEI) [8,9]. Oxidative decomposition of electrolytes is detrimental since apart from material loss and CEI resistance increase, it is also associated with the electrode cross-talk phenomenon, where transition metals (TMs; Co^{2+}, Ni^{2+}, and Mn^{2+}) dissolve from the cathode and are deposited on the anode [8,10]. Deposited TMs promote electrolyte breakdown, thicken the solid electrolyte interphase (SEI), and increase the possibility of high surface area lithium (HSAL) plating. HSAL is particularly detrimental since it consumes active lithium, resulting in rapid capacity fade, known as roll-over failure [11,12].

Another strategy to increase energy density is by incorporating silicon into the anode [13,14]. To deal with the large volume change during lithiation, silicon is usually added as SiOx and mixed with graphite to form a SiO_x-graphite composite with up to 20 wt.% of SiO_x [1,13]. Even with this approach, the SEI is still prone to break down due to the SiO_x volume changes [12]. Consequently, a robust SEI layer is necessary to avoid lithium loss from continuous SEI re-formation, which would result in a severe capacity fade.

The combined challenges associated with the cathode and anode greatly impair cycling stability. To address this issue, a protective coating layer on both electrodes to form protective CEI and SEI has been

---

* Corresponding author.
E-mail address: Philip.Niehoff@uni-muenster.de (P. Niehoff).

https://doi.org/10.1016/j.ensm.2024.103735
Received 12 June 2024; Received in revised form 9 August 2024; Accepted 21 August 2024

proposed [15,16]. Lower Li^+ conductivity, scalability challenges, and high costs often come as drawbacks [17]. An alternative strategy involves developing novel electrolytes to form robust SEI and CEI in vivo [18–21]. These electrolytes include (localized) high-concentration electrolytes [19,22,23], ethylene carbonate (EC)-free electrolytes [6, 24], fluorine-rich electrolytes [8,25,26], and electrolytes with multi-functional additives [6,10,18,27].

The use of electrolyte additives (1–10 wt.%), in particular, is one of the most effective and commonly employed methods to enhance the stability of LIBs due to the possibility of maintaining the chemical, electrochemical, and physical characteristics of the state-of-the-art (SOTA) electrolytes [28,29]. In LIB with SiO_x-containing anodes, fluoroethylene carbonate (FEC) is commonly used as an additive in the electrolyte to enable the formation of an effective SEI [30]. Nevertheless, FEC cannot inhibit TM dissolution from the cathode and is unstable under the presence of dissolved TMs [31,32,33]. The decomposition of PF_6^- anion, as well as TMs dissolution, affects FEC stability and produces various compounds, *e.g.*, HF, H_3OPF_6, HPO_2F_2, H_2PO_3F, and H_3PO_4, through a defluorination mechanism triggered by the Lewis acidic PF_5 generated from the decomposition of $LiPF_6$ [32,33]. To enhance the stability of FEC, various additives, including $LiN(SO_2CF_3)_2$, $LiSO_3CF_3$ salts, Tris(pentafluorophenyl)borate (TPFPB) [33], HF scavenger amino-silane-containing hexamethyldisilazane (HMDS), (trimethylsilyl) isothiocyanate (TMSNCS) [32], and lithium difluorophosphate (LiDFP) [6,18,34], have been introduced. However, the practical application of these additives may be limited due to their synthesis complexity and toxicity [35–37].

Prior study on graphite/$LiNi_{0.5}Co_{0.2}Mn_{0.3}O_2$ cells cycled at 4.5 V vs. Li $|Li^+$ that SDM offers unique functionality by simultaneously protecting both the graphite anode and $LiNi_{0.5}Co_{0.2}Mn_{0.3}O_2$ cathode at high voltage (4.5 V vs. Li $|Li^+$), using a combination of detailed electrochemical methods and ex-situ surface analyses to elucidate the improved performance of graphite/$LiNi_{0.5}Co_{0.2}Mn_{0.3}O_2$ cells. However, it did not provide insights into the scavenging ability of SD, such as scavenging H_2O and HF from the SOTA electrolyte. Additionally, we believe that graphite is much more stable in $LiPF_6$ in EC/EMC cells, whereas SiO_x is incompatible with $LiPF_6$-based electrolytes, the chemical instability of the lithium hexafluorophosphate causes hydro-fluoric acid to develop, which targets the native SiOx layers on silicon anodes and breaks the chemical bond to the carboxymethylcellulose sodium salt binder. Thus, this study introduces the use of sulfonyl diimidazole (SD) as a co-additive of FEC for NMC811||SiO_x-Gr operated to 4.5 V. The additive not only safeguards the SEI by scavenging HF and H_2O but also protects the electrodes by forming sulfonyl-containing interphases [38]. Furthermore, the imidazole component, which acts as a Lewis base, aids in the neutralization of acidic gaseous byproducts, such as PF_5, HF, and CO_2, that are produced during the decomposition of the electrolyte [39, 40]. In this paper, we thoroughly examine the properties of SD alongside FEC. We extensively explain how SD facilitates the high performance of NMC811||SiO_x-Gr cells at 4.5 V and 1C cycling. This research emphasizes the relevance of electrolyte additives in preventing sudden cell failure when applied at high voltages.

2. Results and discussion

Fig. 1a gives the density functional theory (DFT) calculation results of plausible reduction pathways of SD and FEC. The reduction potential of SD was evaluated for the neutral molecule (SD only) and the SD coordinated to a lithium ion (SD-Li^+) in order to qualitatively assess the impact of the intermolecular electrolyte environment on the reduction potential. The reduction potential for the neutral molecule is calculated to be 2.3 V vs. Li|Li^+. In the SD-Li^+ dimer, the presence of the lithium ion favors reduction, yielding a potential of 2.9 V. This enhancement is attributed to the lithium ion stabilizing the negative charge of the added electron. Additionally, it facilitates the fragmentation of SD in the SD-Li^+ complex, stabilizing the product side and resulting in a notably high reduction potential of 4.3 V vs. Li|Li^+. However, it's important to note that the last reaction, involving bond breaking between sulfonyl and

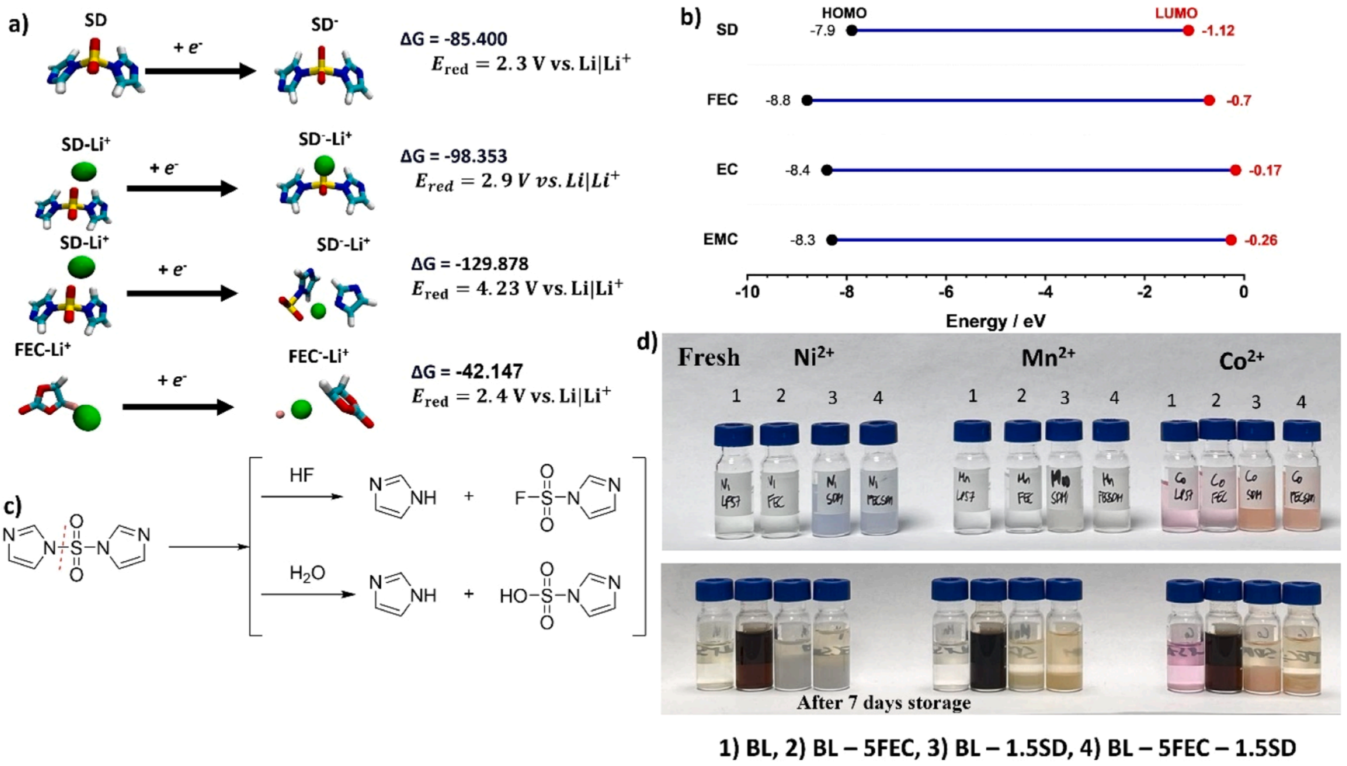

Fig. 1. a) Possible reaction paths, associated free energy differences ΔG (computed at 298 K) in kcal mol^{-1}, and reduction potentials E_{red} in V vs. Li|Li^+ of SD and FEC. b) calculated HOMO and LUMO energies in eV of SD, FEC, EC, and EMC. c) illustration of the scavenging effect of SD. d) TM scavenging experiment of BL, BL – 5FEC, BL – 1.5SD, and BL – 5FEC – 1.5SD electrolytes.

diimidazole, is likely kinetically slow, requiring activation energy. The reduction potential for FEC is relatively modest but positive, approximately 0.2–0.3 V vs. Li|Li$^+$ (as depicted in Figure S1a). This remains largely unchanged when a lithium ion is added to stabilize the negative charge post-reduction. Furthermore, akin to SD, the reduction potential significantly rises when considering the fragmentation reaction leading to LiF formation from FEC (as illustrated in Figure S1d and Fig. 1a).

Fig. 1b displays the DFT-calculated energy levels for the lowest unoccupied molecular orbital (LUMO) and highest occupied molecular orbital (HOMO) of SD and FEC additives, as well as EC and EMC solvents. The LUMO level of SD is calculated to be −1.12 eV, which is notably lower than that of ethylene carbonate (EC, −0.17 eV), ethyl methyl carbonate (EMC, −0.26 eV), and FEC (−0.7 eV). This suggests a preference for the reduction of SD over FEC, EC, and EMC. Consistent with the findings of Jankowski and Weiling *et al.* [20,41], it is demonstrated that the presence of an aromatic ring decreases the LUMO and elevates the HOMO levels, thereby reducing the HOMO-LUMO gap. This suggests that the SEI and cathode electrolyte interphase (CEI) formed on the surfaces of SiO_x-Gr and NMC811, respectively, should contain inorganic-rich compounds.

Fig. 1c depicts the proposed mechanism of SD bond cleavage into imidazole and sulfonyl groups, depicted through the DFT calculation in Fig. 1a. This occurs due to the minimum electrostatic potential near the N and S-N facilitating nucleophilic and electrophilic reactions. Consequently, the imidazole part attracts H^+, while the sulfonyl group attracts F^- ions, scavenging HF and PF_5 [32,33]. To confirm SD scavenging ability, we conducted DFT calculations, as shown in Figure S2. The computed reaction energies for the two scavenging reactions depicted below are relatively small or even negative (particularly with H_2O), indicating that both reactions are thermodynamically feasible. Therefore, we believe that these reactions, along with the IC—CD and GC–MS results, substantiate the interaction between FEC and SD. While SD scavenges HF and H2O, FEC protects the SiOx-Gr negative electrode.

To assess the impact of incorporating SD into the SOTA electrolyte with FEC, the electrolytes underwent a 7-day storage period with transition metal (TM) ions (Ni^{2+}, Mn^{2+}, and Co^{2+}) to simulate TM dissolution from the cathode into the electrolyte. As seen in Fig. 1d, color change was observed in the baseline electrolyte with FEC (BL-5FEC) electrolyte, indicating the formation of acidic products due to FEC decomposition, exacerbated by the presence of transition metal additives. This decomposition leads to the breakdown of PF_6^- anions, resulting in the generation of various acidic compounds such as HF, H_3OPF_6, HPO_2F_2, H_2PO_3F, and H_3PO_4 [32]. However, the presence of SD in BL – 5FEC electrolyte, *i.e.*, BL – 5FEC – 1.5SD, acts as a protective barrier against FEC degradation by scavenging HF and stabilizing the electrolyte's acidity through sulfonyl and imidazole functional groups. No color change was observed in BL – 5FEC – 1.5SD electrolytes under the presence of TM ions. (Fig. 1d).

2.1. Electrochemical performance

Fig. 2a presents the overcharge experiment results, comparing the oxidative stability of the electrolytes on a working electrode with a practical surface area, *i.e.*, $LiNi_{0.5}Mn_{1.5}O_2$ (LNMO) [42,43].. The LNMO

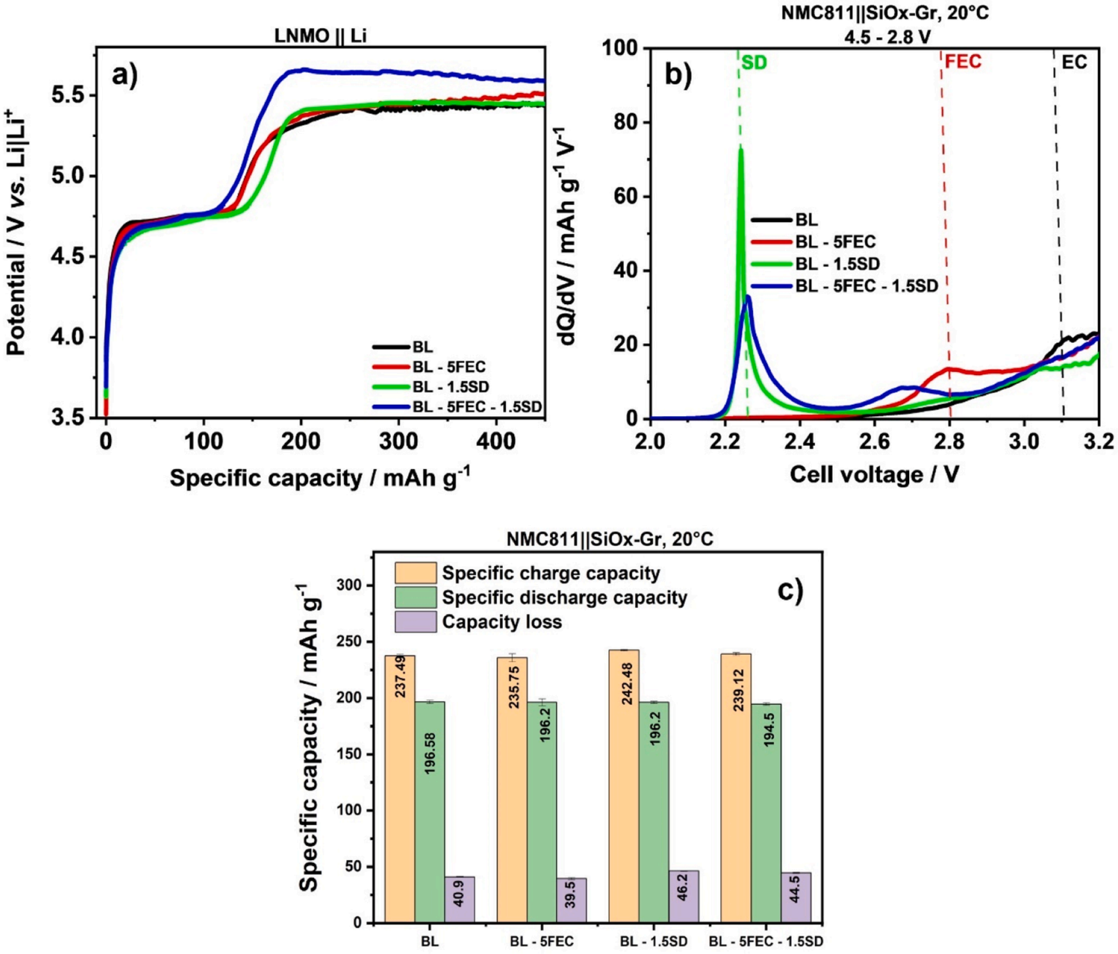

Fig. 2. a) Overcharge experiments of LNMO electrodes comparing the oxidative stability of electrolytes, b) first cycle (C/10) differential capacity vs. voltage plots, c) first-cycle specific charge and discharge capacity, as well as capacity loss of additives in NMC811||SiOx-Gr cells. All experiments were carried out with at least 3 cells.

electrode was chosen for the overcharge experiment because it represents a more application-relevant system with conditions similar to those used in practical applications, such as Ni-containing and high-voltage composite electrodes during galvanostatic overcharge. During charging, LNMO undergoes delithiation within the potential range of 4.65 – 4.9 V vs. $Li|Li^+$ in the cases of all electrolyte systems. BL, BL–5FEC, and BL–1.5SD electrolytes exhibit similar plateaus at 5.4 V vs. $Li|Li^+$, attributed to bulk electrolyte oxidation. In contrast, BL–5FEC–1.5SD electrolyte demonstrates enhanced stability under high-voltage conditions, with an elevated anodic stability of 5.65 V vs. $Li|Li^+$, attributed to the over-voltage of interphase formation in the presence of FEC and SD additives

To gain a better understanding of the electrolyte reduction behavior during SEI formation, differential capacity (dQ/dV) vs. cell voltage plots are shown in Fig. 2b. In the case of the BL electrolyte, the first reduction peak is observed at a cell voltage of ≈ 3.1 V, which can be attributed to the reduction of EC on the surface of the negative electrode. The introduction of 5 wt% FEC into the BL electrolyte prevents the decomposition of EC due to the earlier reduction of FEC at ≈ 2.8 V. In contrast, Ghaur *et al.* showed that EC reduction proceeds when only 2 wt% of FEC is added to the electrolyte [30]. Introducing SD into the BL electrolyte (BL–1.5SD) results in a strong reduction peak at ≈ 2.24 V and an additional broad peak at 3.04 V. The first peak can be attributed to the decomposition of the SD. In contrast, the second broad peak can be attributed to the decomposition of the EC, suggesting that SD-derived SEI does not fully eliminate EC decomposition. Finally, the introduction of FEC and SD into the BL electrolyte (BL – 5FEC – 1.5SD) shows reduction peaks at ≈ 2.26 V and ≈ 2.67 V, which can be attributed to the reductive decomposition of SD and FEC, respectively. In this electrolyte, SD reduction onset remains the same as in BL–1.5SD, while FEC reduction happens at a lower onset compared to that in BL-5FEC electrolyte, which indicates an interaction of the two additives. In addition, no EC peak is observed when FEC and SD are employed.

The first-cycle specific capacities of NMC811||SiO_x-Gr cells charged to 4.5 V are depicted in Fig. 2c. Cells containing BL exhibited a discharge capacity of ≈196 ± 0.4 mAh g^{-1}, with a specific capacity loss of ≈ 40 ± 0.4 mAh g^{-1}. Similar capacity loss is observed when FEC is introduced to the BL electrolyte. Nevertheless, the capacity loss increases to 46 and 45 mAh g^{-1} in the case of BL-1.5SD and BL-5FEC-1.5SD electrolytes, respectively. However, the discharge capacities are still comparable for all electrolytes. This implies that SD decomposition products are reduced and oxidized simultaneously during charge, not leading to an increase in charge capacity but not causing additional irreversible Li loss [39].

Finally, the various electrolytes' self-discharge behavior was examined to investigate the film formation properties further. Despite this, Schmiegel *et al.* and Ghaur *et al.* have shown that NMC523||SiO_x-Gr cells containing FEC suffer from rapid self-discharge after storage for >300 h. In our cell systems, all investigated electrolytes showed a comparable voltage fading with no abrupt decrease (Figure S3) [30,44].

Following the initial electrochemical evaluation of the additives in NMC811||SiO_x-Gr cells, as depicted in Figs. 1 and 2, the additives underwent an extended galvanostatic charge/discharge cycling at elevated voltage and 1C. Previously, Klein *et al.* demonstrated the exceptional high-voltage performance of NCM523||Graphite lithium-ion cells by adding 1 wt.% of lithium fluorophosphate (LiDFP) into the SOTA electrolyte system. The mechanism behind LiDFP's superiority over other commercial additives, such as VC and FEC, was explained using IC—CD (Ion chromatography: conductivity detection) and XPS [6,31]. The study showed that LiDFP can effectively scavenge transition metals from the electrolyte and counteract electrode crosstalk, thereby preventing sudden cell failure [6]. Furthermore, Tan *et al.* utilized LiDFP additive in a Li||$LiNi_{0.76}Mn_{0.14}Co_{0.10}O_2$ cell, resulting in a capacity retention of 97 % of the initial capacity (235 mAh g^{-1}) after 200 cycles. This remarkable performance was attributed to the robust interphase on the cathode formed by the decomposition of lithium difluorophosphate [18]. The catalytic effect of transition metals facilitates this decomposition, and the resulting decomposition products (Li_3PO_4 and LiF) form a protective interphase [18]. Inspired by these abovementioned works, LiDFP was employed in NMC811||SiO_x-Gr pouch cells, as shown in Figure S6. Introducing 1.5 wt% LiDFP into the BL electrolyte system delayed the abrupt failure of the cell. However, it was found that LiDFP was not a suitable additive for SiO_x-Gr-based negative electrodes, as evidenced by the capacity degradation that occurred after approximately 80 cycles. This could be attributed to the instability of the SEI on the SiO_x-Gr negative electrode. Thus, the challenges of cycling high-voltage silicon-based LIBs lead us to explore novel additives. Therefore, the electrochemical cycling experiments were conducted to investigate the impact of SD as an electrolyte additive on high-voltage NMC811|| SiO_x-Gr cell chemistry. To optimize the right amount of SD additive, 1, 1.5, and 2 wt% SD were first subjected to long-term cycling at 4.5 V with a 1C charge and discharge rate. As shown in Fig. 3a, the addition of 1 and 2 wt.% SD leads to a sudden capacity failure of the cells roughly after 60 cycles, whereas the addition of 1.5 wt.% SD, although the nature of the fading mechanism is the same, delayed the sudden failure of the cells to roughly 75 cycles. After this initial assessment, 5 wt% FEC was introduced into 1. 1.5 and 2 wt% SD as a dual additive. As shown in Figure S4 by cell voltage vs. specific capacity during SEI formation (first cycle), all BL-5FEC-1SD, BL-5FEC-1.5SD, and BL-5FEC-2SD delivered discharge capacities of 197 mAh g^{-1}, 194 mAh g^{-1}, and 186 mAh g^{-1} respectively. The discrepancy could be due to increased resistances with higher SD content as during formation the discharge capacity was comparable. Based on the initial assessment, the BL electrolyte was evaluated without and with FEC and SD additives.

The long-term cycling performance of NMC811||SiO_x-Gr in BL and BL–5FEC shows a sudden failure as early as 45 cycles, while the capacity drop is delayed to 75 cycles in the case of the BL–1.5SD electrolyte system. The observed capacity degradation and roll-over failure may indicate the presence of high surface area lithium (HSAL) metal deposition on the SiO_x-Gr-based anode induced by transition metals dissolution and subsequent deposition on the anode surface [6,45]. In contrast, the cells cycled with the BL–5FEC–1.5SD prevented the accelerated capacity fading of NMC811||SiO_x-Gr with an initial capacity retention of 92 % after 100 cycles, as depicted in Fig. 3b.

Early presence of Li metal dendrite formation at the SiO_x-Gr negative electrode, known as HSAL, can lead to a strong drop in Coulombic efficiency (C_{Eff}) and fluctuations of the specific charge capacity. Fig. 3c shows a fluctuation of Ceff in the BL and BL-5FEC electrolyte systems. However, despite the drop-in capacity explained above, the BL-1.5SD electrolyte does not exhibit any fluctuation of Ceff. Furthermore, Fig. 3d further indicates the presence of HSAL as there is an abnormal increase of specific charge capacities, which correlates with the onset of roll-over fading.

The average charge and discharge voltage difference (ΔV) can provide insights into the polarization of the cells. Additionally, it could be used to investigate the sudden capacity fading of cells [46]. As shown in Fig. 3e, for cells containing BL and BL-5FEC, despite lower cell polarization during the first 45 cycles, a rapid increase in ΔV was observed exactly at the onset of roll-over. In contrast, cells containing BL–1.5SD and BL–5FEC–1.5SD electrolytes can withstand such polarization. Although numerous factors can influence the impedance buildup of cells, the large volume change of silicon, electrolyte/active Li consumption due to SEI thickening, electrolyte oxidation at the positive electrode, and a shuttle-type reaction, transition metals dissolution (TMD) can be a reason for the impedance growth in cells containing BL and BL-5FEC electrolyte systems operated at 4.5 V [44,45]. Additionally, as shown in Figure S5, the impedance buildup for cells cycled with BL and BL-5FEC electrolytes is significantly higher compared to BL-5FEC-1.5SD. This aligns with the polarization plot and TOF-SIMS investigation shown in the section below, which indicated a thinner SEI when FEC-SD is used.

In summary, it was found that using the new additive formulation,

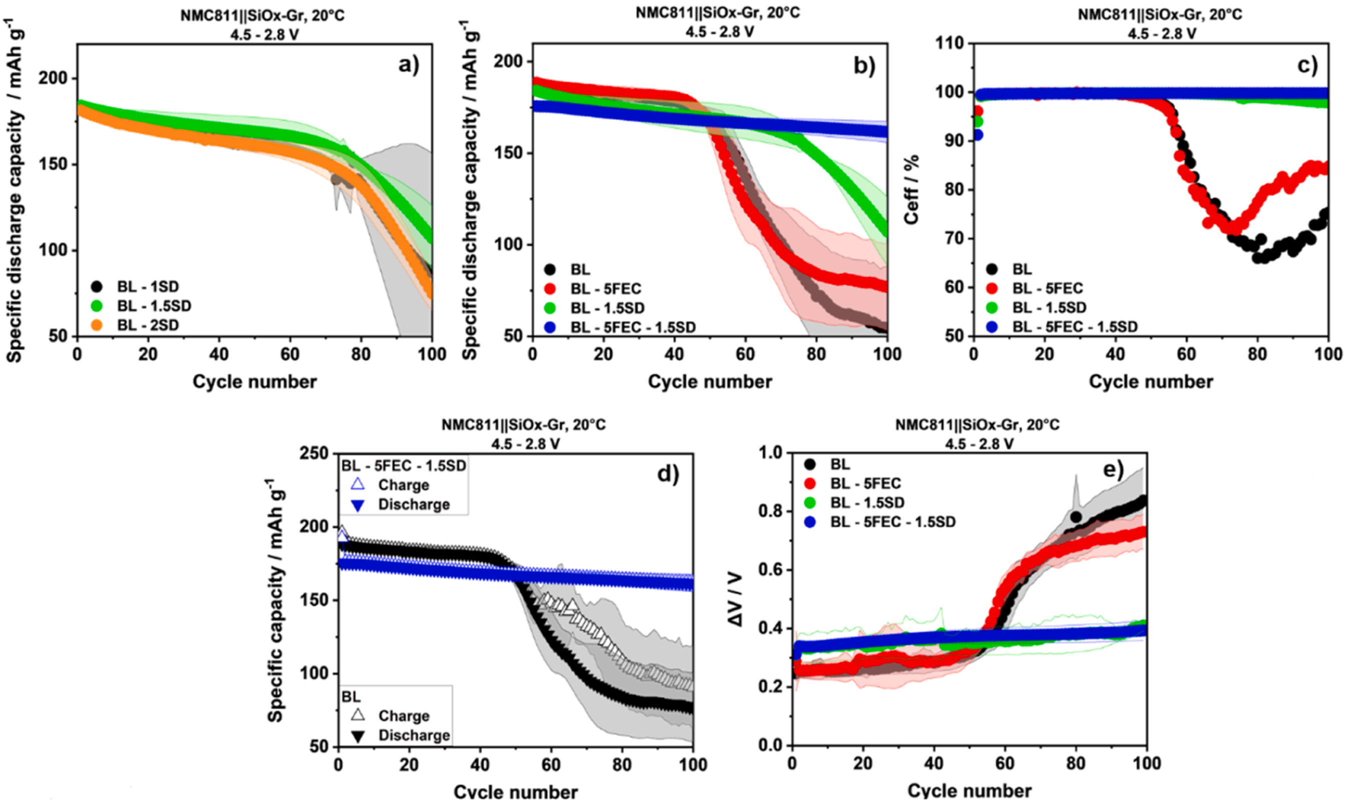

Fig. 3. a) Specific discharge capacity vs. cycle number plots for BL electrolytes with different amounts of SD, b) specific discharge capacity, c) Coulombic efficiency, d) specific charge and discharge capacity. e) average charge and discharge voltage difference (ΔV) vs. cycle number of NMC811||SiO_x-Gr cells cycled at 1 C with BL, BL – 5FEC, BL – 1.5SD and BL – 5FEC – 1.5SD electrolytes. Here, 1C is defined as 190 mA g^{-1}. Shaded areas represent the standard deviation of 3 cells.

which prevents the reduction of EC resulted in remarkable performance for both NMC811||SiO_x-Gr and NMC811||Gr pouch cells. This is likely due to the excellent film-forming ability of SD that suppresses the dissolution of transition metals into the electrolyte, thus giving protection of FEC and facilitating a smooth FEC-based SEI formation on the anode through scavenging of impurities in the BL electrolyte [32]. Additionally, SD and FEC form a stable, robust, and uniform film on SiO_x-Gr and Gr-based negative electrodes.

2.2. Anode investigation by SEM

To better understand the different capacity fading behaviors of cells cycled with different electrolytes, SiO_x-Gr anodes were extracted from NMC811||SiO_x-Gr cells after 100 cycles and after discharging to 2.8 V. Subsequently, scanning electron microscopy (SEM) images were taken. As seen in the optical photograph of the SiO_x-Gr electrode extracted from the NMC811||SiO_x-Gr pouch cells in Fig. 4a-c, shiny deposits, which are attributed to Li metal deposits, are observed over the anode surfaces from cells with BL, BL-5FEC, and BL-1.5SD. These shiny deposits are also found to stick to the separators in Figure 4a-c. Notably, the introduction of SD into the BL electrolyte visually suppresses the amount of the shiny deposit (Fig. 4c), and a complete suppression of the deposition is observed when BL-5FEC-1.5SD was employed (Fig. 4d).

Low magnification SEM images in Fig. 4a-c reveals that the SiO_x-Gr surfaces cycled with BL, BL-5FEC, and BL-1.5SD electrolytes are covered by a large amount of decomposition products, indicated by the changed particle morphology compared to the pristine (Figure S10). This contrasts with the almost unchanged particle morphology of the anode from cells cycled with BL–5FEC–1.5SD shown in Fig. 4d. Moreover, the high magnification SEM images in Fig. 4a-c reveal the presence of shiny and chunky particles, likely to be metallic Li, on SiO_x-Gr surfaces cycled with BL, BL - 5FEC, and BL-1.5SD. This is, again, not observed on SiO_x-Gr cycled with BL–5FEC–1.5SD. Furthermore, the electrode cycled with BL and BL-5FEC-1.5SD electrolyte systems show an even distribution and minimal accumulation of lithium and transition metals (Mn, Co, and Ni), as depicted in Figure S11. The presence of lithium could still be due to lithiated graphite particles in the discharged state and lithium from SEI components, such as LiF. In contrast, the anode cycled with BL electrolyte exhibits a highly uneven and significant accumulation of lithium metal and transition metals, as shown in Figure S11a. LA-ICP-MS analysis indicated that using the BL electrolyte with FEC and SD additives for NMC811||SiOx-Gr cells with an upper cut-off voltage of 4.5 V significantly reduced the transition metal dissolution and deposition (TMDMD) on the SiOx-Gr anode surface.

2.3. Interphase investigation by ATR-FTIR spectroscopy and TOF-SIMS

Attenuated total reflection Fourier-transform infrared spectroscopy (ATR-FTIR) was utilized to analyze the SEI composition of SiO_x-Gr anodes taken from NMC811||SiO_x-Gr after 100 cycles. Fig. 5a and Figure S13 shows noticeable differences in the SEIs formed with or without the electrolyte additive SD. Notably, distinct bands corresponding to vibrational modes associated with functional groups of the SD (Table S2), i.e. the symmetric stretching (ν_s) of $O = S = O$ at 1433 cm^{-1}, the wagging deformation (δ_{wag}) of $O = S = O$ at 634 cm^{-1}, and C—N-C at 608 cm^{-1}, were detected. The presence of these bands on anodes cycled with BL–SD (Fig. 5a) and BL–5FEC–1.5SD (Figure S13) suggests the integration of the SD fragments into the SEI of these anodes. Additionally, the absence of a pronounced band at 1152 cm^{-1}, linked to the asymmetric stretching (ν_{as}) of the S-N-S bond of SD, on the cycled anode with SD additive hints at the possible breakdown of this bond. Furthermore, the bands that can be assigned to the imidazole ring and the SO_2 group are present (δ_{wag} C—N-C, d_{wag} C—H, δ_{sc} $O = S = O$, u_{as} $O = S = O$); however, the bands that can be assigned to the N-S-N vibration

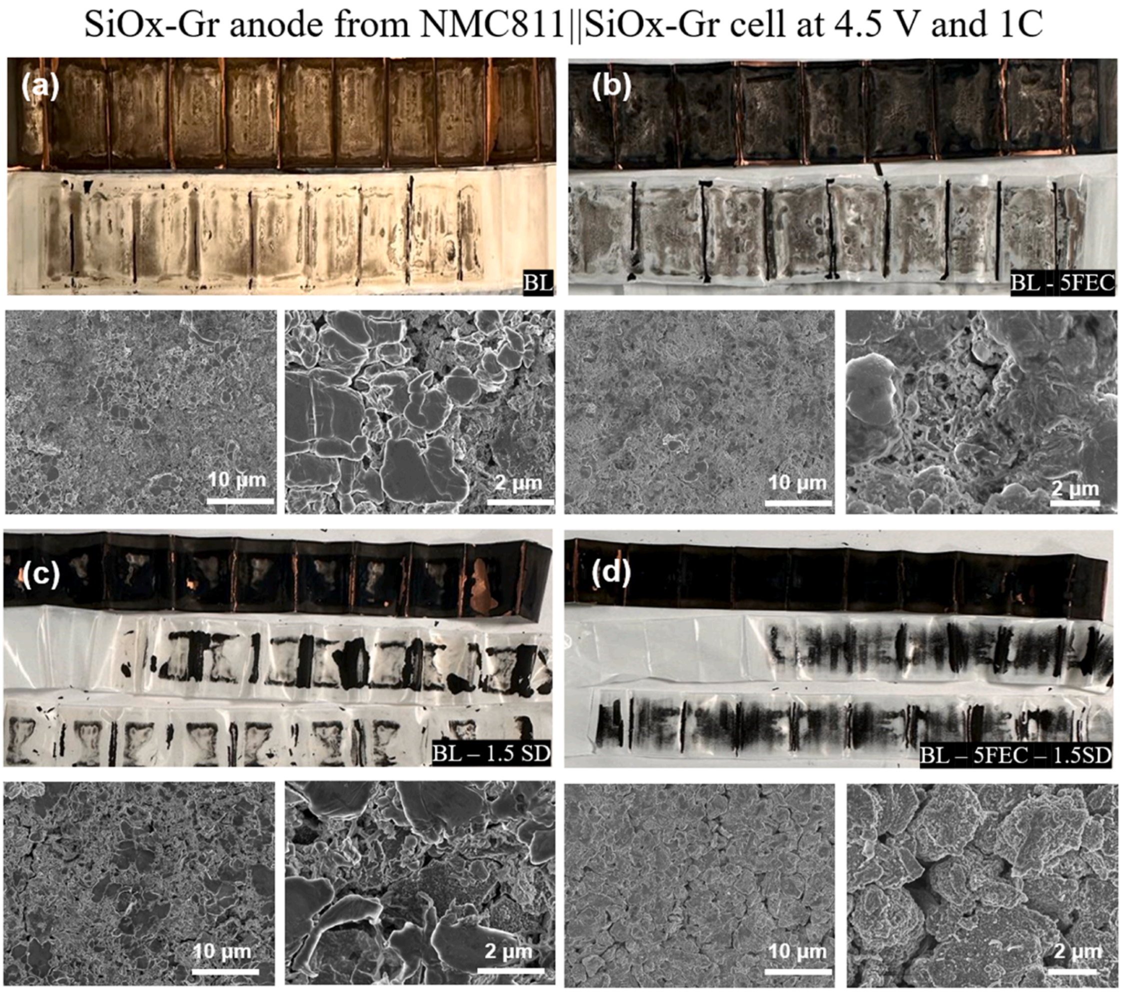

Fig. 4. Optical photograph and SEM images of SiO_x-Gr anodes after 100 cycles in NMC811||SiO_x-Gr cells with a) BL, b) BL–5FEC, c) BL–SD, and d) BL–5FEC–1.5SD electrolytes.

are absent. This supports the conclusion that the SD degrades on the surface due to the breaking of the NSN bond.

Regarding the possible degradation products of SD shown in Fig. 1c, no prominent IR band associated with the O—H bond (at 3600 cm^{-1}) from SDOH (Imidazole-1-sulfonic acid) is detected (Table S4). The reason could be that, in fact, no organic SEI components with OH-groups are present in the SEI, as these are mostly present as O-Li; this component might be present in the SEI in the dehydrogenated but lithium-coordinated state. In contrast, the presence of a band at 749 cm^{-1}, which can be assigned to S-F bond stretching by DFT calculations, suggests the presence of SDF (Imidazole-1-sulfonyl fluoride) as an SD decomposition product (Table S4). This assignment of the S-F bond stretching is further supported by comparing SDF to the bis(fluorosulfonyl)imide (FSI) anion, which shares a similar molecular structure in terms of the S-F bond [47]. Although the reported FSI IR band of S-F is around 790, the heterocyclic aromatic(resonance) side of the SD additive (compared to FSI), the conjugated effect would lower the wavenumber of the S-F band. Therefore, the calculated IR value of SDF and the experimented value is lower. The inclusion of fluorine in SDF supports the initial hypothesis of the HF scavenging capability of the sulfonyl group (Fig. 1c). Consequently, SDF is incorporated into the SEI during cycling. In contrast to the noticeable differences observed on the anode, no extra bands that can be definitively attributed to SD were detected in the cycled cathode, (Figure S12) indicating a more pronounced impact of SD in the anode.

Additionally, regarding corroboration of these band assignments, we performed highly accurate DFT calculations of SD and the degradation products with the results given in the Table S2–4. By this, the putative underlying vibration modes of SD, SDF, and SDOH were assigned and the important vibrations are highlighted in the spectra in the manuscript. Furthermore, the complementary IC—CD-MS shown in the subsequent section of analysis of the electrolytes shows the presence of structures f and g, which are also formed by breaking of the NSN bond. The breaking of the SD at the N-S bond is indicated by the absence of the two bands assigned by DFT calculations to N-S-N stretching. One might argue the band is overlapped by SEI bands formed by BL. However, the spectrum of the pristine SD shows that the NSN stretching bands exhibit similar intensities compared to the deformation bands or the SO_2 stretching bands. Thus, similar intensity ratios should be expected in the interphase spectrum, but this is not observed. This indicates the proposed breaking of the molecule at the NSN bond in the interphase. Consequently, as a result of SD and its degradation products along with FEC a stable, robust and thin interphases were formed. The correlation between impedance growth and interphase thickness is well-supported. As shown in Fig. 3e and Figure S5, the impedance growth closely aligns with the SEI and CEI thicknesses indicated by TOF-SIMS .

Time of flight-secondary ion mass spectrometry (ToF-SIMS) was utilized to gain deeper insights into the components and thickness of the SEI and CEI. In Fig. 5b-e, 80 % Si signal intensity was chosen as a criterion for when the SEI is sputtered through and the bulk SiO_x-Gr particle is reached [12]. As such longer sputter times signify a thicker SEI layer. The negative fragments ion Li^- indicates the organic and

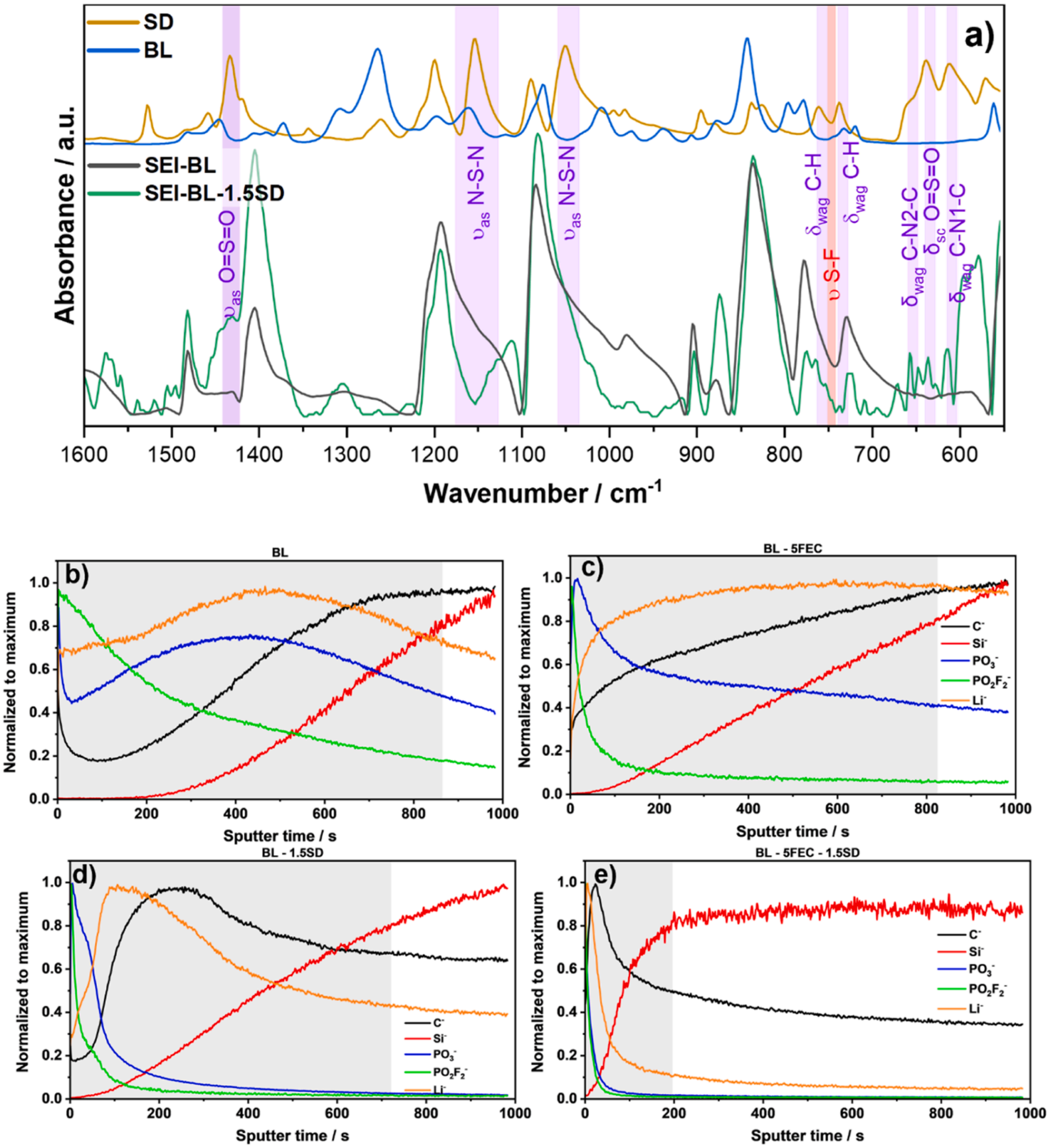

Fig. 5. a) ATR-FTIR spectra of the bulk electrolytes, bulk SD additive, and the interphases of the cycled SiO_x-Gr anodes with and without additives (SD (powder) orange, (SD (SEI, green), BL (SEI, black) and BL(Pristine); b-e) normalized ToF-SIMS depth profile of SiOx-Gr anodes. All electrodes were harvested from fully discharged NMC811||SiOx-Gr cells after 100 cycles.

inorganic Li salts in the SEI and PO_3^- and $PO_2F_2^-$ represent conducting salt decomposition products. Consequently, higher relative PO_3^- and $PO_2F_2^-$fragment ion signal intensity indicate a greater level of $LiPF_6$ decomposition within the SEI. The use of BL electrolyte notably results in the formation of thick SEI, with a maximum for $LiPF_6$ decomposition products inside the SEI, suggesting hydrolysis and subsequent $LiPF_6$ decomposition during cycling (Fig. 5b). The anode cycled in BL - 5FEC also indicates a thick SEI, though a reduced amount of $PO_2F_2^-$ fragments compared to BL is observed (Fig. 5c). The use of BL – 1.5SD slightly reduces the SEI thickness and notably suppresses the amount of PO_3^- and $PO_2F_2^-$ within the SEI (Fig. 5d). Finally, the anode cycled with BL – 5FEC – 1.5SD electrolyte is found to have the thinnest SEI, with $LiPF_6$ decomposition products being most visible at the surface of the SEI, indicating a stable SEI with low interfacial resistance. Mn^+ fragment ions were also found to be below the limit of detection for the BL – 5FEC – 1.5SD electrolyte compared to the other electrolytes, indicating the suppression of electrode crosstalk (Table S1). This aligns well with the remarkable improvement of cycling performance and the lack of decomposition product observed with SEM, enabled by the dual additive approach.

Finally, It can therefore be concluded that the precise composition of SEI on SiOx-Gr comprises F, N, and S, as evidenced by the anode that was cycled with FEC-SD containing electrolyte. This indicates that SD and FEC are implicated in the formation of the surface film on the SiOx-Gr anode, resulting from their preferential reduction. To substantiate this assertion, ATR-FTIR and TOF-SIMS analyses were conducted, as illustrated in Fig. 5a-e, in conjunction with DFT simulations that corroborate this conclusion.

To investigate the impact of electrolytes on the CEI, ToF-SIMS chemical maps were performed on cross-sectionally polished positive electrode sheets obtained from NCM811||SiO_x-Gr cells after 100 cycles (Fig. 6a-c). As the measurement was conducted in a discharged state, it is evident that Li is present in the bulk of the NCM811 particle. In all cases, the images depict a double-sided NMC811 cathode cross-section. The

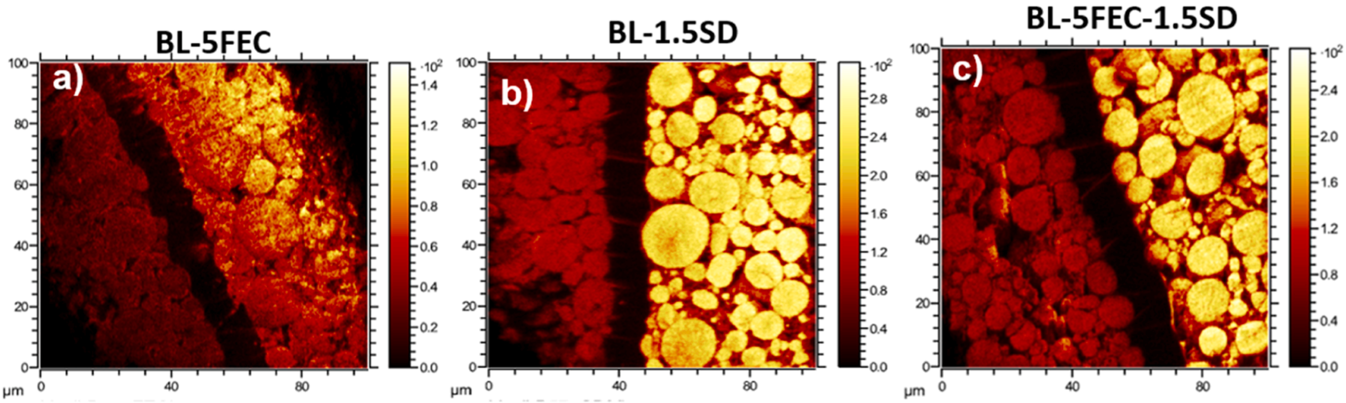

Fig. 6. a-c) cross-section TOF-SIMS chemical maps of Li$^+$ secondary ions on double-layered NMC811 cathodes. All electrodes were harvested from fully discharged NMC811||SiOx-Gr cells after 100 cycles.

right side of all images has higher intensities compared to the left side due to the direct contact of the former with the sample holder, resulting in a lower surface charging effect. While the cross-sectional image of electrode sheets cycled with BL – 5FEC shows hardly visible CAM particles (Fig. 6a), those cycled with both SD-containing electrolytes exhibit clear CAM particle outlines (Fig. 6b-c). This could be attributed to a thicker CEI, in the case of the cells cycled with BL – 5FEC and thinner CEIs for cells cycled with BL – 1.5SD and BL – 5FEC – 1.5SD.

2.4. Ex situ IC-CD-MS bulk analysis of aged electrolyte

After 100 cycles, *post mortem* analysis by means of ion chromatography-conductivity detection-mass spectroscopy (IC—CD-MS) and gas chromatography-mass spectroscopy (GC–MS) was conducted to analyze the decomposition of the electrolytes. As shown in Fig. 7a, the aged BL electrolyte contains 4 different peaks attributed to the degradation products of LiPF$_6$, such as organophosphates (area a) and PO$_2$F$_2^-$ (area d). Moreover, HF is also formed as the hydrolysis product of LiPF$_6$, as indicated by the F$^-$ peak in Fig. 7b [48,49]. In aged BL – 5FEC electrolyte, IC-MS results show a pronounced increase in PO$_2$F$_2^-$peak intensity compared to the BL electrolyte (Fig. 7a, area d), suggesting a more severe LiPF$_6$ decomposition under the presence of FEC, likely involving PF$_5$ Lewis acid- or HF-induced dehydrofluorination of FEC, generating various acids such as HF, HPO$_2$F$_2$, H$_2$PO$_3$F, and H$_3$PO$_4$ [33]. The presence of F^- and HPO$_2$F$_2^-$ and H$_2$PO$_3$F$^-$ ions is further supported by the IC—CD results in Fig. 7b. Fig. 7a further reveals that the introduction of SD, results in the formation of fluorosulfonyl compound (area f), showing the HF-scavenging effect of SD.

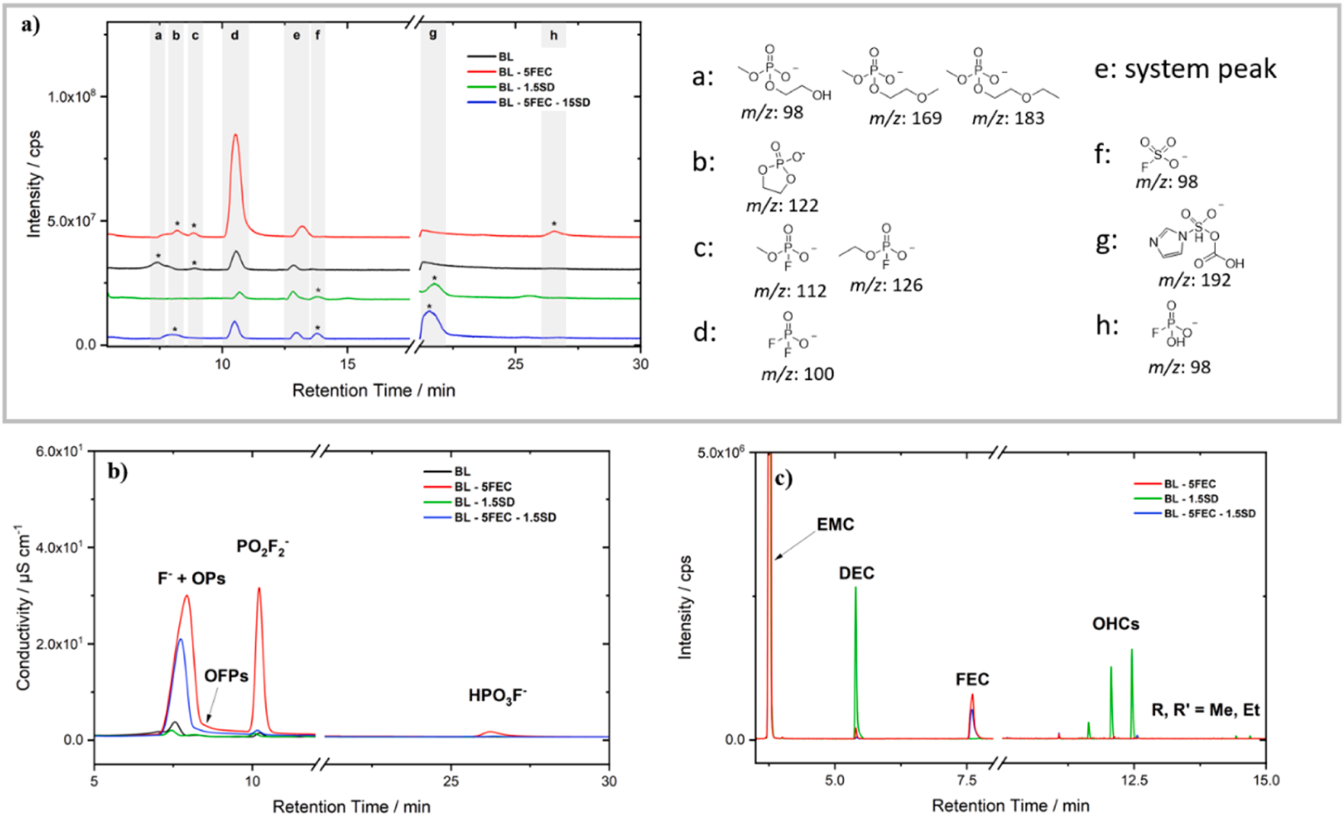

Fig. 7. a) IC-MS, b) IC—CD, and c) GC–MS results of BL, BL – 5FEC, BL – 1SD, and BL – 5FEC – 1.5SD electrolytes extracted from in NMC811||SiO$_x$-Gr pouch cells at 4.5 V after 100 cycles. The areas marked with letters in a) correspond to the possible structures shown in the right part.

Moreover, gas chromatography-mass spectrometry (GC–MS) analyses were conducted to investigate the formation of volatile decomposition/ aging products in the electrolyte. The formation is based on the electrochemical reduction of EMC and EC at negative electrode in a first step. This provokes the formation of lithium alkoxides among others. These compounds can react by nucleophilic attacks with EMC to the observed transesterification products or with EC to the observed ‘OHCs This formation of trans-esterification and oligomerization products resulting from the decomposition of SOTA solvents in the BL electrolyte serves as indirect evidence of SEI formation [30]. In the BL electrolyte system, these trans-esterification and oligomerization products also referred to as ’OHCs (DMC, DEC, ethylmethyl-2,5-dioxahexane-carboxylate (EMDOHC), dimethyl-2,5-dioxahexane-carboxylate (DMDOHC), and diethyl-2, 5-dioxahexane-carboxylate (DEDOHC)), are observable, as depicted in Fig. 7c According to literature, these species have been found to correlate with parasitic reactions, which worsen electrochemical performance and contribute to increased impedance growth [50].. As illustrated in Fig. 7c, compared to the BL electrolyte blend, both BL-5FEC and BL-5FEC-1.5SD notably eliminated the products observed when using the BL electrolyte. However, incorporating without FEC in the BL electrolyte did not prevent the formation of these trans-esterification and oligomerization products. These findings align well with the observations of the aforementioned electrochemical results. The ability of 5FEC-1.5SD to prevent roll-over may be attributed to the formation of stable, uniform, and thin interphase films before the reduction of EC and EMC.

Finally, the introduction of SD to the BL or BL – 5FEC electrolyte is found to greatly reduce $LiPF_6$ decomposition, as seen by the notable reduction of $PO_2F_2^-$ (Fig. 7a, area d and Fig. 7b) and F- + organophosphates (Fig. 7b).

3. Discussion

The dQ/dV plot in Fig. 1b reveals that the SEI composition includes S, N, and F components, resulting from the sequential decomposition of additives, starting with SD and followed by FEC. In this context, SD serves a dual purpose: it acts as a film-forming additive and protects FEC from decomposition, thereby preventing the formation of acidic products. To verify these findings, ATR-FTIR and IC-MS analyses were conducted. Fig. 5 shows the absence of two bands associated with N-S-N stretching (as determined by DFT calculations), suggesting the breakdown of SD at the N-S bond. While one might argue that these bands could be masked by SEI bands formed by BL, this is unlikely. The pristine SD spectrum shows comparable intensities for the NSN stretching bands and the deformation or SO_2 stretching bands. If the NSN bond remained intact in the interphase, similar intensity ratios would be expected, but this is not observed. This evidence supports the proposed cleavage of the SD molecule at the NSN bond within the interphase. Regarding SD’s scavenging effect, IC-MS results for the aged BL-5FEC electrolyte (Fig. 7a, area d) show a marked increase in $PO_2F_2^-$ peak intensity compared to the BL electrolyte, as illustrated in Fig. 5. The observed results indicate increased LiPF6 decomposition when FEC is present. This likely involves PF_5 Lewis acid or HF-induced dehydrofluorination of FEC, generating various acids including HF, HPO_2F_2, H_2PO_3F, and H_3PO_4. The IC—CD results in Fig. 7b further support the presence of F^-, $HPO_2F_2^-$, and $H_2PO_3F^-$ ions.

Fig. 7a demonstrates that adding SD leads to fluorosulfonyl compound formation (area f), showcasing SD’s HF scavenging capability. To validate this scavenging ability, DFT calculations were performed (Figure S2). The computed reaction energies for two scavenging reactions are relatively small or negative (especially with H_2O), suggesting both reactions are thermodynamically possible. These calculations, along with IC—CD and GC–MS results, support the interaction between FEC and SD. In this system, SD scavenges HF and H_2O, while FEC protects the SiOx-Gr negative electrode. Fig. 6c shows that both BL-5FEC and BL-5FEC-1.5SD significantly reduced the products observed with the BL electrolyte. However, adding SD without FEC to the BL electrolyte did not prevent trans-esterification and oligomerization products. These findings align with the previously mentioned electrochemical results. The ability of 5FEC-1.5SD to prevent roll-over may be due to the formation of stable, uniform, and thin interphase films prior to EC and EMC reduction. Our research also highlighted SD’s effect on the conducting salt’s decomposition under specific cycling conditions. This decomposition wasn’t prevented by using the baseline electrolyte or FEC alone. However, adding SD to either the BL or BL-5FEC electrolyte significantly reduced $LiPF_6$ decomposition, as evidenced by the marked decrease in $PO_2F_2^-$ (Fig. 6a, area d and Fig. 6b) and F^+ organophosphates (Fig. 6b). Fig. 6a further demonstrates that introducing SD leads to the formation of a fluorosulfonyl compound (area f), illustrating SD’s HF scavenging effect. Our findings were corroborated by complementary studies using TOF-SIMS, EIS, and LA-ICP-MS. The thicker SEI observed through EIS and TOF-SIMS suggests that the film formed by SD and FEC decomposition is both stable and thin. Moreover, LA-ICP-MS revealed reduced transition metal (TM) deposition on SiOx-Gr when SD was present. This reduction can be attributed to SD’s ability to scavenge HF, which would otherwise cause TM corrosion and subsequent dissolution. This observation further supports SD’s dual role as both a scavenging and film-forming additive.

4. Conclusion

This study offers an in-depth analysis of the impact of sulfonyl diimidazole (SD) as a co-additive for protecting FEC-based SEI in high-voltage NMC811||10SiO_x-Gr cells. Electrochemical and *post mortem* analyses reveal that the use of 1 M $LiPF_6$ in EC/ EMC mixture with the addition of 1.5 wt% SD and 5 wt% FEC prevents roll-over failure in cells operated at 20 °C to 4.5 V. It is found that FEC is necessary to enable stable SEI formation in the SiO_x-containing cells used in this study. Nevertheless, high voltage operation of these cells exacerbates FEC decomposition, initiated by PF_5 Lewis acid and HF, resulting in the formation of various acidic compounds. As a result, large amounts of TMs are deposited on the SiO_x-Gr anode. This catalyzes solvent decomposition, thickens the SEI, and increases the risk of Li plating. The scavenging effect of SD suppresses the formation of acidic products associated with the decomposition of FEC. Consequently, low amounts of TM deposits are present on the anode and Li plating is eliminated. This finding holds important implications for designing electrolytes for SiO_x-containing lithium-ion cells operating at high voltages. A co-additive that is capable of preventing FEC decomposition is necessary to prevent roll-over failure in these cells.

5. Experimental section

5.1. Electrolyte preparation

The reference electrolytes were prepared by dissolving 1 M $LiPF_6$ in EC: EMC (3:7 by weight “$LiPF_6$ in EC/EMC” electrolyte); all components were purchased from Targray (ENCHEM, purity: battery grade). The electrolyte additives, lithium difluorophosphate (LiDFP, American Elements; CAS No.: 24,389–25–1; purity: ≥99.9 %), fluoroethylene carbonate (FEC, ENCHEM, purity: battery grade) and 1,1′ -sulfonyldiimidazole (SD, TCI America; CAS No: 7189–69–7; >98% purity) were added to the electrolyte solution with concentrations of wt. %. All the electrolytes were prepared in the argon-filled glovebox with H_2O and O_2 levels below 1 ppm. The electrolytes were stirred for 5 h using a magnetic stirrer to ensure complete dissolution of the salt. In order to simulate the TM dissolution during the scavenging experiment that may occur from NMC811,TM salts were added to the electrolyte. Powders of thermally stablenickel(II) bis(trifluoromethanesulfonyl) imide (Ni(TFSI)2) (purity: ≥97 %),cobalt(II) bis(trifluoromethanesulfonyl)imide (Co(TFSI)2) (purity: ≥97 %),and manganese(II) bis(trifluoromethanesulfonyl)imide (Mn(TFSI)2) (pu-rity: ≥97 %) (Alfa Aesar) salts were dissolved in the electrolyte so that theconcentration of each metal cation was 15 mm.

(2) (PDF) Assessing Key Issues Contributing to the Degradation of NCM-622 || Cu Cells: Competition Between Transition Metal Dissolution and “Dead Li” Formation. Available from: https://www.researchgate.net/publication/380,365,619_Assessing_Key_Issues_Contributing_to_the_Degradation_of_NCM-622_Cu_Cells_Competition_Between_Transition_Metal_Dissolution_and_Dead_Li_Formation [accessed Jul 21, 2024].

5.2. Electrochemical investigations

200 mAh NMC811||SiO_x-Gr and NMC811||Gr LiFun cells (LiFun Technologies Xinma Industry Zone, Golden Dragon Road, Tianyuan District, Zhuzhou City, Hunan Provence, PRC, 412,000) balanced to 4.5 V were used for electrochemical investigations. NMC811 positive electrodes consist of 96.4 wt% active material, 1.6 wt% carbon black, and 2 wt% polyvinylidene difluoride (PVdF) binder. The negative electrodes consist of 94.8 wt% artificial graphite/silicon oxide composite active material (90 %AGr, 10 % SiO_x and 90 %AGr, 10 % SiO_x), 1.4 wt% carbon black as a conductive agent, and 1.3 wt% sodium-carboxymethyl cellulose (CMC) and 2.5 wt% styrene-butadiene rubber (SBR) binders. The cathode mass loading was ≈13.9 mg cm^{-2}. The mass loading for the anode was ≈8 mg $cm_{.}^{-2}$ Before cell assembly, the cells were opened and dried under reduced pressure at 90 °C overnight. Subsequently, the pouch cells were filled with 700 µL of electrolyte, which corresponds to 200 mAh nominal capacity at 0.1C of the used pouch cells. Finally, the cells were vacuum-sealed at 15 % of the ambient pressure using GN—HS350V from Gelon Lib Co., Ltd., China, while maintaining a gas pocket in a dry room with a dew point of less than −50 °C.

NMC811||SiO_x-Gr and NMC811||Gr full cells were cycled using a Maccor 4000 battery testing system and constant current (CCCV) charge/discharge cycling in a cell voltage range of 4.5 – 2.8 V. For formation protocols, C/10 and C/5 charging and discharging rates were applied in a cell voltage range of 4.5–2.8 V. After that, the cells were subjected to 1C long-term cycling. Following each current charge, a constant voltage (CV) step was done until the specific current dropped below C/20. All electrochemical experiments were conducted in climate chambers at a constant temperature of 20 °C. The detailed mechanism of these pouch cells’ drying and sealing process was explained elsewhere [20,30].

For storage experiments, the pouch cells were connected to the cell test equipment (MACCOR 4000 Series) at a temperature of 60 °C (in a temperature-controlled chamber with a tolerance of ± 0.1 °C) after the SEI formation. The cells were stored for 6 h at open circuit voltage (OCV) and then charged to the upper cut-off voltage of 4.5 V. The OCV was measured for 720 h once the current dropped below 0.02C. The cells were discharged to the lower cut-off voltage of 2.8 V at a rate of 100 mA. Subsequently, the pouch cells charged and discharged in the first cycle between 2.8 and 4.5 V at 0.1C, followed by four cycles between 2.8 and 4.5 V at 0.5C. A constant voltage step was applied at the top of the charge until the current dropped below ≈0.02C to initiate the discharge. For this experiment, whole procedure was adopted from[30,44]

Overcharge experiments were conducted in T-cells (Swagelok) using a three-electrode setup. The working electrode was a $LiNi_{0.5}Mn_{1.5}O_2$-based composite electrode (Ø12 mm) with an areal capacity of approximately 0.36 mAh cm^{-2}. The electrode consisted of 90 wt.% active material, 5 wt.% carbon black (Super C65, Imerys Graphite & Carbon), and 5 wt.% poly(vinylidene difluoride) binder (Solef 5130, Solvay) coated on aluminum foil. The counter and reference electrodes consisted of lithium foil (500 µm; Gelon Lib Group) with Ø12 mm and Ø8 mm diameters, respectively. The working and counter electrodes were separated by three layers of Ø12 mm polypropylene (PP) fiber separators (FS2190; Freudenberg) soaked in 120 µL of electrolyte. The reference electrode was separated by two layers of the same separator soaked in 120 µL of electrolyte. Pouch cells and T-cells were assembled in a dry room atmosphere with a dew point of at least −50 °C (0.16 % relative humidity).

After allowing the T-cells to rest for 3 h post-assembly to ensure adequate electrolyte wetting, overcharge experiments were initiated. The cells were charged using a CC mode (0.09 mA cm^{-2}), and the working electrode’s potential was continuously monitored. Charging was stopped upon reaching either 30 h of measurement time or 6 V. To ensure reproducibility, at least two T-cells per electrolyte mixture were employed.

5.3. Scanning electron microscopy (SEM)

SEM imaging was used to examine the surface morphology of the cycled SiO_x-Gr anodes and NMC811 cathodes after 100 cycles in a cell voltage range of 4.5–2.8 V (Carl Zeiss AURIGA; Carl Zeiss Microscopy GmbH). EDX was performed at an accelerating voltage of 20 kV using an X-MaxN 80 mm^2 EDX detector (Oxford Instruments). The INCA software was used to assess the spectra (Oxford Instruments). The cells were disassembled in the argon-filled glove box (H_2O and O_2 level below 1 ppm) to avoid contact with atmospheric air. Before the analysis, the cathode and anode surfaces were rinsed with 1 mL of dimethyl carbonate (DMC). Details about the procedure can be found elsewhere [51].

Density rfunctional theory (DFT) calculations were conducted using the Gaussian16 package [52]. The optimization of molecular structures employed the B3LYP DFT functional and the 6–311++G(3df, 2p) basis set. To simulate the influence of an electrolyte environment, an SMD implicit solvation model with parameters specific to acetone was chosen for its similarity in dielectric constant to liquid carbonate-based electrolytes [53–56]. Following geometry optimization, the calculated infrared (IR) frequencies and intensities of SD, SDF, and SDOH molecular structures were utilized to support the assignment of bands in the ATR-FTIR spectra. The outcomes, including frequency scaling factors of 1 and 0.98 and potential assignments, are detailed in the supplementary information.

5.4. Attenuated total reflection Fourier-transform infrared spectroscopy (ATR-FTIR)

Analysis of the interphases was conducted using an Invenio-R FT-IR spectrometer (Bruker) with a Platinum-ATR unit (diamond crystal, Bruker) and a mercury-cadmium-telluride (MCT) detector inside a custom-build glovebox under nitrogen flux. The spectra were acquired with a spectral resolution of 4 cm^{-1} at an incidence angle of 45° Each spectrum was obtained by accumulating 32 interferograms for background and sample spectra, respectively. The spectra are presented as absorbance and were processed by concave rubber band background correction (15 iterations, straight lines). Further details of this method can be found elsewhere [20].

5.5. Time of flight-surface ion mass spectroscopy (ToF-SIMS)

Measurements were performed using an IONTOF ToF-SIMS 5 spectrometer utilizing a 30 keV Bi nanoprobe in both spectrometry (bunched) mode fast imaging mode with delayed extraction to enable high lateral and mass resolution. In bunched mode, the primary ion gun was set to shoot Bi_3^{2+}-ions with an ion current of 2 pA over an area of 100 µm × 100 µm with a resolution of 128 × 128, and the analyzer was set to negative ion mode, and a cycle time of 60 µs. Bunched mode was combined with a 1 keV Ar sputter gun to obtain depth information. For depth profiling, the Ar^+ sputter beam was set to sputter at an ion current of 250 nA over an area of 300 µm × 300 µm in interlaced mode. Each sample was probed at three different locations to validate the results. The target current was measured before and after each measurement to compensate for fluctuations in the primary and sputter ion currents. Fast imaging was performed on an ion milled cross-section over an area of 100 µm × 100 µm with a resolution of 1024 × 1024. A binning of 4 pixels was used to increase contrast. To avoid contact with air, the samples were transferred to and introduced into the ToF-SIMS device using an airtight sample carrier purchased from IONTOF. The samples were prepared for ToF-SIMS depth profiling by washing the surface of the electrode five times with DME to remove any excess electrolyte and conducting salt that may interfere with the measurement.

5.6. Ion chromatography-conductivity detection-mass spectrometry (IC—CD-MS)

A qualitative analysis of anionic degradation products was executed on an 850 Professional IC (Metrohm, Switzerland) with conductivity detection (CD) hyphenated to an 6530 Accurate Mass Quadrupole-Time-of-Flight (Q-TOF)-MS (Agilent, USA). A Metrosep A Supp 7 column (250×4.0 mm, 5 μm; Metrohm) with a Metrosep A Supp 5 Guard/4.0 guard column was used for an isocratic separation of the anionic compounds at an oven temperature of 65 °C and an applied flow rate of 0.7 mL min-1 over a total runtime of 30 min. All samples were diluted 1:1000 with acetonitrile and the injection volume was set to 65 μL. The eluent consisted of a 3.6/3.4 mM Na2CO3/NaHCO3 aqueous solution and acetonitrile in a ratio of 58:42 (v/v). The utilized suppressor was sequentially regenerated by 0.1 M sulfuric acid and rinsed with MilliQ Water. Ionization in the MS was performed in ESI(-) mode at a capillary voltage of 3.5 kV. The nebulizer gas was set to 45 psi and the drying gas to a flow of 10 L min-1 at 350 °C. A collision-induced dissociation energy of 30 eV was applied for MS/MS experiments and the mass range was set to *m/z* 70–500 in MS1 and *m/z* 50–500 in MS2. Instrument control, data acquisition, and data evaluation were performed for MS with MassHunter Data Acquisition and MassHunter Qualitative Analysis B.08.00 (Agilent), while for IC with MagIC Net 3.3 (Metrohm).

5.7. Gas chromatography – flame ionization detector (GC-FID)

A qualitative analysis by GC–MS of carbonate-based solvents and decomposition products was executed on a Nexis GC-2030 (Shimadzu) equipped with a non-polar Restek Rxi®−5 ms (30 m x 0.25 mm x 0.25 μm) fused silica column (5 % diphenyl/ 95 % dimethyl polysiloxane). The sample injection was done with a volume of 1 μL at an applied split ratio of 1:10 and a set temperature of 250 °C. Helium (6.0 purity) was used as carrier gas with a column flow of 1.15 mL min-1. The oven program started with an initial temperature of 40 °C which was held for 1 min, followed by a first ramp of 3 °C min-1 to 60 °C and a subsequent second ramp of 30 °C min-1 until a temperature of 260 °C was reached. This final temperature was held for 2 min, resulting in a total measurement time of 16.33 min. The MS operated in the electron ionization (EI) mode with an ion source temperature of 200 °C and an interface temperature of 250 °C, while the filament voltage was set to 70 V and the detector voltage was relative to the respective tuning file. The mass range was set to 20–350 *m/z* with an event time of 0.1 s in scan mode. The identification of compounds was verified with the NIST 11 library. All samples were diluted 1:100 with DCM to precipitate and remove the conductive salt prior to injection.

CRediT authorship contribution statement

Feleke Demelash: Writing – original draft, Methodology, Investigation, Conceptualization. **Anindityo Arifiadi:** Investigation. **Bastian Heidrich:** Writing – review & editing. **Egy Adhitama:** Investigation. **Christian-Timo Lechtenfeld:** Investigation. **Niklas M. Abke:** Investigation. **Matthias Weiling:** Investigation. **Jian Fen Wang:** Investigation. **Diddo Diddens:** Investigation. **Simon Wiemers-Meyer:** Writing – review & editing. **Martin Winter:** Writing – review & editing. **Masoud Baghernejad:** Writing – review & editing. **Philip Niehoff:** Writing – review & editing.

Declaration of competing interest

The authors declare that they have no known competing financial interests or personal relationships that could have appeared to influence the work reported in this paper.

Data availability

Data will be made available on request.

Acknowledgments

The authors thank the Federal Ministry of Education and Research (BMBF) for funding this work in the project “FormEL” (03XP0296B).

Supplementary materials

Supplementary material associated with this article can be found, in the online version, at doi:10.1016/j.ensm.2024.103735.

References

[1] R. Schmuch, R. Wagner, G. Hörpel, T. Placke, M. Winter, Nat. Energy 3 (2018) 267.
[2] X. Wang, Y.-L. Ding, Y.-P. Deng, Z. Chen, Adv. Energy Mater. (2020) 10.
[3] S.-T. Myung, F. Maglia, K.-J. Park, C.S. Yoon, P. Lamp, S.-J. Kim, Y.-K. Sun, ACS. Energy Lett. 2 (2017) 196.
[4] W. Li, E.M. Erickson, A. Manthiram, Nat. Energy 5 (2020) 26.
[5] H.-J. Noh, S. Youn, C.S. Yoon, Y.-K. Sun, J. Power. Sources. 233 (2013) 121.
[6] S. Klein, S. van Wickeren, S. Röser, P. Bärmann, K. Borzutzki, B. Heidrich, M. Börner, M. Winter, T. Placke, J. Kasnatscheew, Adv. Energy Mater. (2021) 11.
[7] K. Kleiner, J. Melke, M. Merz, P. Jakes, P. Nagel, S. Schuppler, V. Liebau, H. Ehrenberg, ACS. Appl. Mater. Interfaces. 7 (2015) 19589.
[8] X. Fan, L. Chen, O. Borodin, X. Ji, J. Chen, S. Hou, T. Deng, J. Zheng, C. Yang, S.-C. Liou, K. Amine, K. Xu, C. Wang, Nat. Nanotechnol. 13 (2018) 715.
[9] P. Xiao, Y. Zhao, Z. Piao, B. Li, G. Zhou, H.-M. Cheng, Energy Environ. Sci. 15 (2022) 2435.
[10] Y. Zhang, Y. Wu, H. Li, J. Chen, D. Lei, C. Wang, Nat. Commun. 13 (2022) 1297.
[11] H. Lee, H.-S. Lim, X. Ren, L. Yu, M.H. Engelhard, K.S. Han, J. Lee, H.-T. Kim, J. Xiao, J. Liu, W. Xu, J.-G. Zhang, ACS. Energy Lett. 3 (2018) 2921.
[12] X. Zhang, Z. Cui, A. Manthiram, Adv. Energy Mater. (2022) 12.
[13] G.G. Eshetu, H. Zhang, X. Judez, H. Adenusi, M. Armand, S. Passerini, E. Figgemeier, Production of high-energy Li-ion batteries comprising silicon-containing anodes and insertion-type cathodes.
[14] E. Adhitama, M.M. Bela, F. Demelash, M.C. Stan, M. Winter, A. Gomez-Martin, T. Placke, On the practical applicability of the Li metal-based thermal evaporation prelithiation technique on Si anodes for lithium ion batteries.
[15] Y. Tesfamhret, R. Younesi, E.J. Berg, Influence of Al 2 O 3 coatings on HF induced transition metal dissolution from lithium-ion cathodes.
[16] L. David, K. Dahlberg, D. Mohanty, R.E. Ruther, A. Huq, M. Chi, S.J. An, C. Mao, D. M. King, L. Stevenson, D.L. Wood, Unveiling the role of Al 2 O 3 in preventing surface reconstruction during high-voltage cycling of lithium-ion batteries.
[17] Q. Wu, S. Mao, Z. Wang, Y. Tong, Y. Lu, Nano Select 1 (2020) 111.
[18] S. Tan, Z. Shadike, J. Li, X. Wang, Y. Yang, R. Lin, A. Cresce, J. Hu, A. Hunt, I. Waluyo, L. Ma, F. Monaco, P. Cloetens, J. Xiao, Y. Liu, X.-Q. Yang, K. Xu, E. Hu, Nat. Energy 7 (2022) 484.
[19] X. Zhang, L. Zou, Y. Xu, X. Cao, M.H. Engelhard, B.E. Matthews, L. Zhong, H. Wu, H. Jia, X. Ren, P. Gao, Z. Chen, Y. Qin, C. Kompella, B.W. Arey, J. Li, D. Wang, C. Wang, J.-G. Zhang, W. Xu, Adv. Energy Mater. (2020) 10.
[20] M. Weiling, C. Lechtenfeld, F. Pfeiffer, L. Frankenstein, D. Diddens, J.-F. Wang, S. Nowak, M. Baghernejad, Adv. Energy Mater. (2023).
[21] J.-G. Han, K. Kim, Y. Lee, N.-S. Choi, Adv. Mater. (Deerfield Beach, Fla.) 31 (2019) e1804822.
[22] X. Cao, H. Jia, W. Xu, J.-G. Zhang, J. Electrochem. Soc. 168 (2021) 10522.
[23] W. Liu, J. Li, W. Li, H. Xu, C. Zhang, X. Qiu, Inhibition of transition metals dissolution in cobalt-free cathode with ultrathin robust interphase in concentrated electrolyte.
[24] Y.-X. Yao, N. Yao, X.-R. Zhou, Z.-H. Li, X.-Y. Yue, C. Yan, Q. Zhang, Ethylene-carbonate-free electrolytes for rechargeable Li-ion pouch cells at sub-freezing temperatures.
[25] L. Ma, S.L. Glazier, R. Petibon, J. Xia, J.M. Peters, Q. Liu, J. Allen, R.N.C. Doig, J.R. Dahn, A guide to ethylene carbonate-free electrolyte making for Li-ion cells.
[26] N. von Aspern, G.-V. Röschenthaler, M. Winter, I. Cekic-Laskovic, Fluorine and lithium: ideal partners for high-performance rechargeable battery electrolytes.
[27] D. Zhang, M. Liu, J. Ma, K. Yang, Z. Chen, K. Li, C. Zhang, Y. Wei, M. Zhou, P. Wang, Y. He, W. Lv, Q.-H. Yang, F. Kang, Y.-B. He, Lithium hexamethyldisilazide as electrolyte additive for efficient cycling of high-voltage non-aqueous lithium metal batteries 2022.
[28] K. Xu, Chem. Rev. 104 (2004) 4303.
[29] K. Xu, Chem. Rev. 114 (2014) 11503.
[30] A. Ghaur, C. Peschel, I. Dienwiebel, L. Haneke, L. Du, L. Profanter, A. Gomez-Martin, M. Winter, S. Nowak, T. Placke, Adv. Energy Mater. (2023) 13.

[31] S. Klein, P. Harte, S. van Wickeren, K. Borzutzki, S. Röser, P. Bärmann, S. Nowak, M. Winter, T. Placke, J. Kasnatscheew, Cell Rep. Phys. Sci. 2 (2021) 100521.

[32] J.-G. Han, M.-Y. Jeong, K. Kim, C. Park, C.H. Sung, D.W. Bak, K.H. Kim, K.-M. Jeong, N.-S. Choi, J. Power. Sources. 446 (2020) 227366.

[33] K. Kim, I. Park, S.-Y. Ha, Y. Kim, M.-H. Woo, M.-H. Jeong, W.C. Shin, M. Ue, S. Y. Hong, N.-S. Choi, Electrochim. Acta 225 (2017) 358.

[34] G. Yang, J. Shi, C. Shen, S. Wang, L. Xia, H. Hu, H. Luo, Y. Xia, Z. Liu, RSC. Adv. 7 (2017) 26052.

[35] T. Dong, S. Zhang, Z. Ren, L. Huang, G. Xu, T. Liu, S. Wang, G. Cui, Adv. Sci. (Weinh) (2023).

[36] H. Moon, H. Nam, M.P. Kim, S.M. Lee, H. Kim, M.H. Jeon, Y.-S. Lee, K. Kim, J.-H. Chun, S.K. Kwak, S.Y. Hong, N.-S. Choi, Adv. Funct. Mater. (2023) 33.

[37] M. Kubot, L. Frankenstein, E. Muschiol, S. Klein, M. Esselen, M. Winter, S. Nowak, J. Kasnatscheew, Lithium difluorophosphate: a boon for high voltage Li ion batteries and a bane for high thermal stability/low toxicity: towards synergistic dual additives to circumvent this dilemma.

[38] A. Eldesoky, A.J. Louli, A. Benson, J.R. Dahn, J. Electrochem. Soc. 168 (2021) 120508.

[39] H. Rong, M. Xu, Y. Zhu, B. Xie, H. Lin, Y. Liao, L. Xing, W. Li, J. Power. Sources. 332 (2016) 312.

[40] M. Nie, J. Xia, J.R. Dahn, J. Electrochem. Soc. 162 (2015) A1186–A1195.

[41] P. Jankowski, M. Poterała, N. Lindahl, W. Wieczorek, P. Johansson, Chemically soft solid electrolyte interphase forming additives for lithium-ion batteries 2018.

[42] J. Kasnatscheew, R.W. Schmitz, R. Wagner, M. Winter, R. Schmitz, J. Electrochem. Soc. 160 (2013) A1369–A1374.

[43] J. Kasnatscheew, B. Streipert, S. Röser, R. Wagner, I. Cekic Laskovic, M. Winter, Phys. Chem. Chem. Phys. PCCP 19 (2017) 16078.

[44] J.-P. Schmiegel, R. Nölle, J. Henschel, L. Quach, S. Nowak, M. Winter, F. Glorius, T. Placke, Cell Rep. Phys. Sci. 2 (2021) 100327.

[45] S. Klein, P. Bärmann, T. Beuse, K. Borzutzki, J.E. Frerichs, J. Kasnatscheew, M. Winter, T. Placke, ChemSusChem. 14 (2021) 595.

[46] J.E. Harlow, S.L. Glazier, J. Li, J.R. Dahn, J. Electrochem. Soc. 165 (2018) A3595–A3601.

[47] M. Kerner, N. Plylahan, J. Scheers, P. Johansson, Thermal stability and decomposition of lithium bis(fluorosulfonyl)imide (LiFSI) salts 2016.

[48] M. Liu, J. Vatamanu, X. Chen, L. Xing, K. Xu, W. Li, ACS. Energy Lett. 6 (2021) 2096.

[49] W. Weber, R. Wagner, B. Streipert, V. Kraft, M. Winter, S. Nowak, Ion and gas chromatography mass spectrometry investigations of organophosphates in lithium ion battery electrolytes by electrochemical aging at elevated cathode potentials.

[50] J. Henschel, C. Peschel, S. Klein, F. Horsthemke, M. Winter, S. Nowak, Angew. Chem. Int. Ed. Engl. 59 (2020) 6128.

[51] E. Adhitama, F. Dias Brandao, I. Dienwiebel, M.M. Bela, A. Javed, L. Haneke, M. C. Stan, M. Winter, A. Gomez-Martin, T. Placke, Adv. Funct. Mater. 32 (2022) 2201455.

[52] M.J. Frisch, G.W. Trucks, H.B. Schlegel, G.E. Scuseria, M.A. Robb, J.R. Cheeseman, G. Scalmani, V. Barone, G.A. Petersson, H. Nakatsuji, X. Li, M. Caricato, A. V. Marenich, J. Bloino, B.G. Janesko, R. Gomperts, B. Mennucci, H.P. Hratchian, J. V. Ortiz, A.F. Izmaylov, J.L. Sonnenberg, Williams, F. Ding, F. Lipparini, F. Egidi, J. Goings, B. Peng, A. Petrone, T. Henderson, D. Ranasinghe, et al., Gaussian 09, Revision, C.01, Wallingford, 2016.

[53] F. Pfeiffer, D. Diddens, M. Weiling, L. Frankenstein, S. Kühn, I. Cekic-Laskovic, M. Baghernejad, Quadrupled cycle life of high-voltage nickel-rich cathodes: understanding the effective thiophene-boronic acid-based CEI via operando SHINERS.

[54] O. Borodin, M. Olguin, C.E. Spear, K.W. Leiter, J. Knap, Towards high throughput screening of electrochemical stability of battery electrolytes.

[55] D.S. Hall, J. Self, J.R. Dahn, Dielectric constants for quantum chemistry and Li-ion batteries: solvent blends of ethylene carbonate and ethyl methyl carbonate.

[56] A.V. Marenich, C.J. Cramer, D.G. Truhlar, Universal solvation model based on solute electron density and on a continuum model of the solvent defined by the bulk dielectric constant and atomic surface tensions.